The Journal of the Acoustical Society of America

NOVEMBER 11 2026

Diffraction by finite-impedance barriers for extended, partially coherent noise sources

Tyce W. Olaveson ; Kent L. Gee

Check for updates

J. Acoust. Soc. Am. 160, 4161–4174 (2026)
https://doi.org/10.1121/10.0047519

View Online
Export Citation

Articles You May Be Interested In

Sound power from a collection of monopoles with arbitrary coherence: Theory and application to aeroacoustic noise sources

J. Acoust. Soc. Am. (February 2026)

Similarity spectra analysis of a lab-scale afterburning jet noise rig

J. Acoust. Soc. Am. (December 2025)

An investigation of the influence of the geometrical parameters of a passive traffic noise barrier upon the noise reduction response

AIP Conf. Proc. (December 2018)

22 November 2026 18:10:11

ASA
LEARN MORE
Advance your science and career as a member of the
Acoustical Society of America

ASA
ACOUSTICAL SOCIETY OF AMERICA

JASA ARTICLE

Diffraction by finite-impedance barriers for extended, partially coherent noise sources

Tyce W. Olaveson[a] and Kent L. Gee
Department of Physics and Astronomy, Brigham Young University, Provo, Utah 84602, USA

ABSTRACT:
This work develops an analytic model for acoustic diffraction by finite barriers of arbitrary impedance from an extended, partially coherent noise source. The barrier impedance is incorporated through transmission and reflection coefficients obtained from standard layer analysis, while finite-barrier effects are modeled by extending analytic diffraction solutions to allow for multiple edges. The formulation is expressed in a transfer-matrix framework that maps source strengths to the radiated pressure field and is generalized to partially coherent sources using cross-spectral matrices. This framework is applied to an example problem that explores the potential of a curtain of bubbly water as a jet noise reduction mechanism for nearby launch personnel. While such a curtain can reduce noise significantly, the acoustic impact of bubbles is negligible under realistic conditions. A best-case scenario is also examined by treating the barrier as an anechoic surface. Under this ideal scenario, it is shown that noise reduction is fundamentally limited by diffraction. Finally, the importance of including coherence in the source description is discussed in the context of the radiated field. © *2026 Acoustical Society of America*.
https://doi.org/10.1121/10.0047519
(Received 13 May 2026; revised 9 September 2026; accepted 12 October 2026; published online 11 November 2026)
[Editor: Xun Huang] Pages: 4161–4174

22 November 2026 18:10:11

NOMENCLATURE

In this paper, boldface is used for vector and matrix quantities, while regular script identifies scalar or field quantities. Some variables have both a scalar and vector representation depending on context. Superscripts are reserved for quantities represented by the same variable when applicable. Subscripts are reserved to identify individual components of a vector or matrix quantity.

- a Bubble radius.
- $\boldsymbol{C}$ Cross-spectral matrix at defined field locations.
- $\boldsymbol{k}^{(n)}$ The nth generic wavenumber with $n = 1, 2, 3$ for regions involved in the barrier calculation.
- p^n The nth generic pressure field, type denoted by superscript.
- q^n The nth generic source strength, type denoted by superscript.
- $\boldsymbol{r}_i^n$ Cartesian coordinates of the ith position of type $n \in \{f, s, r\}$ for field, source, and reflection.
- R Pressure reflection coefficient.
- $\mathcal{R}^n$ The nth region surrounding the barrier, type denoted by superscript.
- $\boldsymbol{S}$ Source cross spectral matrix.
- T Pressure transmission coefficient.
- Z^n The nth generic transfer function, type denoted by superscript
- $\mathcal{Z}^n$ The nth transfer function masked by region of existence, type denoted by superscript.
- θ^n Angle of specular reflection or transmission, type denoted by superscript

[a]Email: tyceolaveson@gmail.com

I. INTRODUCTION

Noise radiation from high-performance, military jets poses a significant risk of hearing loss for launch personnel on aircraft carriers (Martens and Spyropoulos, 2010). For this reason, significant resources have been devoted to developing technologies capable of reducing radiated sound levels (Wall *et al.*, 2022). In general, there are three ways to reduce noise: at the source, at the receiver, or along the propagation path. Noise reduction at the jet noise source has generally taken the form of nozzle modification, such as chevrons (Henderson and Bridges, 2010), that are designed to disrupt radiating turbulent structures. One challenge with nozzle-based noise reduction comes in designing a system that can reduce noise without impacting the overall thrust. Reducing noise at the receiver is generally limited to hearing protection, which comes with its own set of challenges, such as limited efficacy in high-amplitude or broadband sound fields (McKinley *et al.*, 2005). Attempts at active noise control have been proposed (Smith *et al.*, 1996); however, due to the turbulent nature of a jet, global control remains elusive, and local control is limited to low frequencies by the field coherence. Additionally, at sufficiently high amplitudes, acoustical bone conduction may limit the effectiveness of standard hearing protection (see Wever and Bray, 1936 and Corso, 1963). Controlling noise along the propagation path involves lengthening the propagation distance or otherwise changing the medium to attenuate noise. For jet noise control, this would take the form of placing a barrier between the jet and the observer, in which case, diffraction plays a major role (see Kurze, 1974 and Wong *et al.*, 2012).

Analytic expressions for diffraction around barriers began in electrodynamics (see the Appendix D of MacDonald, 1902). Since electromagnetic radiation obeys the Helmholtz equation, the same diffraction principles apply to acoustic radiation, which is just a scalar field case of the more generalized vector diffraction. The original extension from optic to acoustic diffraction was provided by Sommerfeld (1896) who adapted the method of images to handle spherical diffraction around a barrier. Later, the work of Bowman *et al.* (1969) provided an extensive collection of example problems treating electromagnetic and acoustic diffraction around simple shapes for planar, cylindrical, and spherical sources. Nearly all these solutions require a series expansion, which quickly becomes impractical when efficiently designing barriers for noise control. To address this challenge, Maekawa (1968) used approximate solutions to determine a simplified expression for the insertion loss (IL) of a thin, planar barrier in terms of a single parameter known as the Fresnel number. This simplified model has proven useful in engineering applications but comes with its own set of shortcomings for thick barriers (see Pierce, 1974). One limitation of the previous approaches is that the diffracting structure is almost universally assumed to have infinite acoustic impedance. Only a small number of analytic studies relax this condition, such as McIver and Rawlins (1995), who looked at diffraction around a thick barrier with a soft or absorbing end face, and Lax and Feshback (1948), who accounted for an impedance boundary condition with a complex phase shift. For structures with arbitrary impedance, Bowman *et al.* (1969) take a brief aside to discuss how impedance enters the relevant boundary conditions but then continue with the rigid assumption. For empirical applications, Menounou and Asimakopoulos (2021) treat diffraction around an absorptive wedge by separating the primary and reflected fields, then scaling the reflected field by an appropriate reflection coefficient. This approach is taken a step further in Menounou *et al.* (2025), where either face of the wedge is assumed to have an arbitrary reflection coefficient, and the diffracted field is decomposed into four pieces to allow for interactions with either wedge face. Among all these studies, the incident field is generally assumed to take a convenient form, e.g., planar, cylindrical, or spherical waves. While both the impedance and incident field assumptions are warranted in analytic derivations, recent projects looking into jet noise reduction using barriers demand more flexibility in material properties, and by extension, their acoustic impedance. Moreover, a jet is an extended, partially coherent noise source, which cannot be modeled by a single line source or monopole.

For applications to extended sources, linear combinations of the convenient models can be taken together to create a more complicated case; however, this approach assumes that the sources interact coherently, which is not always true. Coherence is a measure of the phase linearity between two signals or waveforms. When there is a constant, consistent phase relationship between two signals, their coherence is one. Any deviation from this relationship degrades the coherence, with a value of zero indicating no phase relationship between the two. The degree to which noise fields interact is determined by their coherence (Jacobsen, 1989; Li *et al.*, 1998). For application to noise sources, the coherence can be defined as an innate quantity, in which case, it describes how well the sources can couple and produce interference phenomena. Partial coherence then impacts how the acoustic fields interact and other overall properties such as the radiated sound power (Olaveson and Gee, 2026).

This paper presents an analytic framework for determining the pressure field generated by an extended, partially coherent noise source in the presence of a barrier with arbitrary acoustic impedance. An analytic framework is desired over a computational scheme partially due to computational speed, but even for a highly optimized numerical process where runtimes are manageable, the primary advantage of the analytic approach is that it can be developed to handle partially coherent noise sources, which is critical to modeling jet noise radiation. To the authors' knowledge, there are no established numerical methods that can implicitly handle a partially coherent noise source. Section II makes up the bulk of the paper and discusses reflection and transmission through a layer with arbitrary impedance. Next, diffraction expressions around semi-infinite barriers are adapted to allow for a finite barrier and then combined with the layer analysis. Finally, the partially coherent and extended nature of the source is accounted for by recasting the problem in terms of cross-spectral matrices (CSMs). The framework is then used to investigate the use of a curtain of bubbly water as a potential jet noise reduction mechanism (see Office of Naval Research, 2025). Section III sets up an example problem of an observer behind a curtain of bubbly water. A previously defined equivalent source model (ESM) that approximates full-scale jet noise is then radiated in the presence of this barrier, and the IL is calculated. While this application shows that the bubbly curtain reduces observed noise, repeating the scenario with a curtain of pure water demonstrates that, in this case, bubbles make a negligible impact on the overall IL. An optimal design is also considered by modeling the barrier as an anechoic surface, which performs better than a water curtain at low frequencies, but is quantitatively similar to water at high frequencies. In the end, jet noise control via barriers is a diffraction-limited problem and research should be focused on controlling flanking paths while maintaining a high-impedance barrier.

II. METHODOLOGY

This section discusses the relevant methods used to determine the pressure field from a partially coherent source in the presence of a barrier of arbitrary impedance. First, reflection and transmission coefficients through a layer of arbitrary impedance are computed using standard layer theory. Next, diffraction around the barrier is computed using analytic expressions from the literature, which are then augmented to allow for diffraction around multiple edges.

22 November 2026 18:10:11

https://doi.org/10.1121/10.0047519

Finally, this section concludes by formulating the equations in terms of CSMs to allow for a partially coherent source description.

A. Reflection and transmission coefficients

In general, when an acoustic wave propagating in one medium is incident on an impedance discontinuity, such as at the boundary between two media, a portion of the energy is transmitted across the discontinuity, while the rest is reflected. Kinsler et al. (1999) provide mathematical relationships describing this behavior, and the discussion provided here is based on their work. A schematic of an acoustic wave incident on such a layer, along with the division of regions surrounding it, is shown in Fig. 1. The layer has a constant thickness s in the x direction and infinite length in the y and z planes.

The acoustic wave is assumed to originate in region 1 and propagates linearly according to its wavevector $\boldsymbol{k}^{(1)} = k_x^{(1)}\hat{\boldsymbol{x}} + k_y^{(1)}\hat{\boldsymbol{y}} + k_z^{(1)}\hat{\boldsymbol{z}}$, where $\hat{\boldsymbol{x}}$, $\hat{\boldsymbol{y}}$, and $\hat{\boldsymbol{z}}$ are unit vectors pointing along their respective axes. The time-harmonic portion, $e^{j\omega t}$, has been omitted, and these results are derived for a steady-state field without loss of generality. At the barrier interface, a portion of the incident energy is reflected as p^r and the rest is transmitted as p^+, which then propagates according to its own wavevector, $\boldsymbol{k}^{(2)}$. This transmitted wave continues until it reaches the back of the layer and a portion is reflected as p^- while the rest is transmitted as p^t. While higher-order reflections exist within the barrier, their aggregate effect in the steady-state can be grouped together into the amplitude coefficients for each wave component: R, A^+, A^-, and T, all of which may be complex. The coefficients R and T are pressure reflection and transmission coefficients, respectively, and they have the relationship

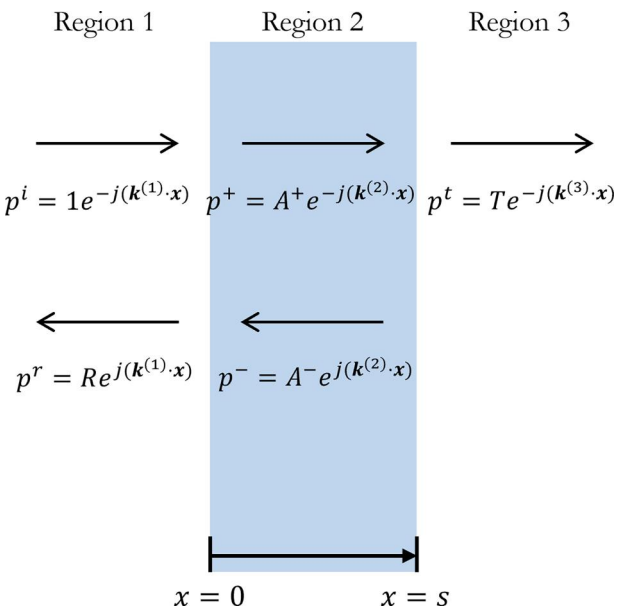

FIG. 1. Regions around a barrier for computing transmission and reflection coefficients.

$|R|^2 + |T|^2 \leq 1$, where a value less than 1 indicates some degree of absorption within the medium.

At each boundary, the pressure and normal particle velocity must be continuous. This leads to a system of four equations

$$\left(p^i + p^r\right)|_{x=0} = \left(p^+ + p^-\right)|_{x=0} \tag{1a}$$

$$\left(\boldsymbol{u}^i + \boldsymbol{u}^r\right)\cdot\hat{\boldsymbol{n}}|_{x=0} = \left(\boldsymbol{u}^+ + \boldsymbol{u}^-\right)\cdot\hat{\boldsymbol{n}}|_{x=0} \tag{1b}$$

$$\left(p^+ + p^-\right)|_{x=s} = p^t|_{x=s} \tag{1c}$$

$$\left(\boldsymbol{u}^+ + \boldsymbol{u}^-\right)\cdot\hat{\boldsymbol{n}}|_{x=s} = \boldsymbol{u}^t\cdot\hat{\boldsymbol{n}}|_{x=s}, \tag{1d}$$

where $\hat{\boldsymbol{n}} = \hat{\boldsymbol{x}}$ is the vector normal to the barrier and $\boldsymbol{u}$ is the appropriate particle velocity. Forms for each of the pressure components are provided in Fig. 1. For a steady-state solution, Euler's equation is used to determine the particle velocity as $\boldsymbol{u} = -(\boldsymbol{k}/\omega\rho)p$. The quantity $\boldsymbol{k}\cdot\hat{\boldsymbol{n}} = \boldsymbol{k}\cdot\hat{\boldsymbol{x}} = k_x$ is positive for rightward-traveling waves, and negative for leftward-traveling waves. For convenience in evaluating the pressure at the boundary between regions 2 and 3, the quantity $E^{\pm} = e^{\pm sk_x^{(2)}}$ is defined to express the phase term that is picked up by propagation across the layer. Evaluating Eqs. (1a)–(1d) yields the following:

$$R - A^+ - A^- = -1, \tag{2a}$$

$$\frac{k_x^{(1)}}{\rho^{(1)}}R + \frac{k_x^{(2)}}{\rho^{(2)}}\left(A^+ - A^-\right) = \frac{k_x^{(1)}}{\rho^{(1)}}, \tag{2b}$$

$$A^+E^- + A^-E^+ - T = 0, \tag{2c}$$

$$\frac{k_x^{(2)}}{\rho^{(2)}}\left(A^+E^- - A^-E^+\right) - \frac{k_x^{(3)}}{\rho^{(3)}}T = 0. \tag{2d}$$

Equations (2a)–(2d) are readily solved for pressure reflection and transmission coefficients.

While this derivation provides the reflected and transmitted normal components for any plane wave with incident angle described by k_x, if the wave were spherical rather than planar, the method of images may be used to approximate the resultant pressure field by replacing the layer with an image source scaled by $R(\theta^r)$ where θ^r is the angle of specular reflection between the source and field point where the pressure is evaluated (see section 6.8 of Kinsler *et al.*, 1999). Of course, the method of images would only be valid for determining field quantities in region 1, and the appropriate transmission coefficient and transmission angles would need to be used for field locations in region 3.

B. Diffraction

In a work aimed at numerical application, Menounou *et al.* (2000) compiled a collection of analytic expressions for diffraction around a semi-infinite barrier. The geometry used in their work is shown in Fig. 2 for a rotated view (a) and a side view (b). The primary source, labeled q^p, is located at (r_0, ϕ_0, z_0) in cylindrical coordinates, where ϕ_0

22 November 2026 18:10:11

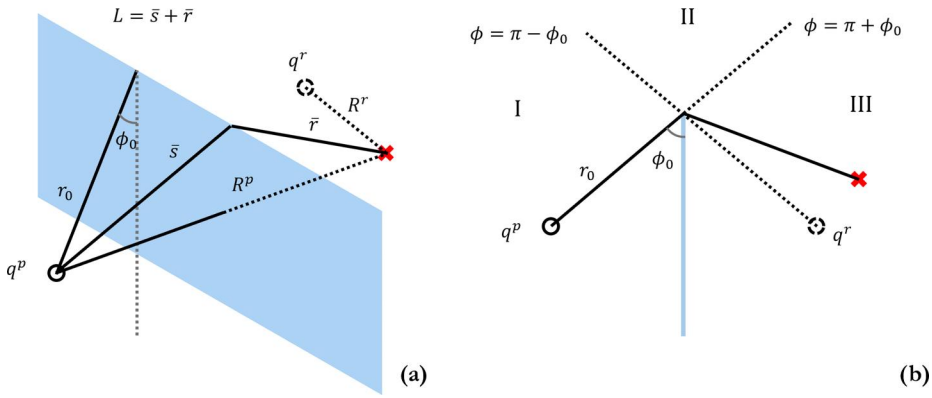

FIG. 2. Geometry for a semi-infinite barrier. Rotated view (a) and side view (b).

and r_0 are measured from the top of the barrier and z_0 is the distance along the barrier from the origin. Without loss of generality, z_0 can be set to zero by placing the origin in-plane with the source. A generic field point [located at (r, ϕ, z)] is marked by a red x, and an image source reflected in the barrier is marked as q^r. The quantity L is the shortest distance between the primary source and the receiver going over the barrier. The quantities R^p and R^r are the shortest distances between the receiver and the primary/image sources respectively, ignoring the barrier. In the right figure, three regions are marked as I, II, and III, respectively. These regions are divided by the geometric shadow zones cast by the primary and image sources and mark where the various pressure fields can exist. In the presence of a semi-infinite barrier, the total pressure field consists of four components: the pressure field generated by the primary source without interacting with the barrier, p^p, the pressure field reflected off the barrier, p^r, the pressure field transmitted through the barrier, p^t, and the pressure diffracted by the edge of the barrier, p^d. Due to the problem geometry, the diffracted pressure is present in all three regions, the primary pressure is present in regions I and II; the reflected pressure is present in region I; and the transmitted pressure is present in region III.

For a spherically incident wave with unit amplitude, the diffracted pressure, p^d, comes in two pieces, one reliant on the primary field, labeled $p^{d,p}$, and one reliant on the reflected field, labeled $p^{d,r}$,

$$p^d = p^{d,p} + p^{d,r}. \tag{3}$$

Each term is defined by

$$p^{d,l} = \operatorname{sgn}(m^{d,l}) \frac{k e^{\mp j\pi/4}}{\sqrt{kL^d}} \frac{e^{jkR^l}}{\sqrt{k(L^d + R^l)}} \left[F(\infty) - F(|m^{d,l}|) \right], \tag{4}$$

where $m^{d,l} = -\operatorname{sgn}\left(\cos\left(\phi^d - \phi_0^d\right)/2\right)\sqrt{k(L^d - R^l)}$, $F(z) = \int_0^z e^{j\pi\tau^2/2} d\tau$ is the Fresnel integral, and $\mp$ is taken to be negative for $l = p$ and positive for $l = r$. The superscript $d \in \{\text{Top}, \text{Left}, \text{Right}\}$ indicates that a quantity is dependent on the geometry of the respective diffraction edge and is included in anticipation of extending to multiple edges. For example, ϕ^{Top} is a generic field angle as measured from the top of the barrier and L^{Right} is the shortest source-edge-receiver distance going around the right edge of the barrier. The superscript $l \in \{p, r\}$ indicates that the parameter is dependent on the primary source or reflected source, respectively, so the variable $m^{\text{Left},r}$ is computed using the positions of the reflected source as measured from the left edge. Equation (4) is valid so long as $kL^d \gg 1$, that is, the shortest source-edge-receiver distance, L^d, is much larger than a wavelength for all edges. Furthermore, the barrier thickness is assumed to be small relative to a wavelength.

The work surrounding Eq. (4) assumes the spherical source provides a unit amplitude pulse; however, the diffracted pressure from a generic source is desired. To accomplish this, the acoustic amplitude $A = (j\rho ck/4\pi)q$ is used to convert from amplitude to a generic volume velocity q. A transfer function can then be defined that acts on this source strength and returns the diffracted pressure as $p^d = Z^d q$. Since the diffracted field depends on the primary and reflected paths, the diffracted transfer function comes in two pieces,

$$Z^d = \sum_{l \in \{p,r\}} Z^{d,l}, \tag{5}$$

where $Z^{d,l} = (j\rho ck/4\pi)p^{d,l}$ is a scaled version of Eq. (4). Menounou *et al.* (2000) showed that if the barrier is instead a pressure release surface (reflection coefficient $R = -1$ for all angles), the summation in Eq. (3) is replaced with a difference. The natural extension of this observation comes from noting that each component of Eq. (5) depends on either the primary or reflected source parameters. Thus, each of the $Z^{d,l}$ terms must operate on the primary or reflected source, respectively, leading to a total diffracted pressure computed as $p^d = \sum_{l \in \{p,r\}} Z^{d,l} q^l$. For the case of a barrier with an arbitrary impedance, the image source can then be scaled by the appropriate reflection coefficient. A similar approach was used by Menounou and Asimakopoulos (2021) when they considered diffraction by absorptive wedges. In their work, the diffracted pressure field was similarly decomposed into two components: a primary and reflected field, where the reflected field was then scaled by the reflection coefficient of the wedge.

22 November 2026 18:10:11

https://doi.org/10.1121/10.0047519

TABLE I. The five regions around the barrier, what conditions must be satisfied for a field point to exist in that region, which pressure fields are present, and a label for where each region exists in relationship to the barrier.

Symbol	Conditions	Pressure fields	Description
$\mathcal{R}^I$	$\phi^d < \pi - \phi_0^d,\ \forall d \in \{\text{Top}, \text{Right}, \text{Left}\}$	$p^p,\ p^r,\ p^{\text{Top}}, p^{\text{Left}},\ p^{\text{Right}}$	Front
$\mathcal{R}^{II}$	$\phi^d > \pi + \phi_0^d,\ \forall d \in \{\text{Top}, \text{Right}, \text{Left}\}$	$p^t,\ p^{\text{Top}}, p^{\text{Left}},\ p^{\text{Right}}$	Back
$\mathcal{R}^{III}$	$\pi - \phi_0^{\text{Top}} < \phi^{\text{Top}} < \pi + \phi_0^{\text{Top}}$	p^p, p^{Top}	Top
$\mathcal{R}^{IV}$	$\pi - \phi_0^{\text{Left}} < \phi^{\text{Left}} < \pi + \phi_0^{\text{Left}}$	p^p, p^{Left}	Left
$\mathcal{R}^V$	$\pi - \phi_0^{\text{Right}} < \phi^{\text{Right}} < \pi + \phi_0^{\text{Right}}$	p^p, p^{Right}	Right

While the expressions for diffraction presented in Menounou *et al.* (2000) are for a semi-infinite wall, the extension to a finite three-dimensional (3D) barrier is straightforward. By exploiting linearity, diffraction around the other two sides of the wall can be accounted for in Eq. (5) by using the appropriate edge-dependent geometric parameters. In this case, there are a total of three diffracted pressure fields. As with the two-dimensional (2D) case, individual pressure fields are not present everywhere around the barrier; thus, regions are defined that limit where each field is present (see Fig. 2). For diffraction around three edges, five natural regions surround the barrier: the front, the back, the top, the left, and the right. As before, these regions are defined by the shadow zones cast by the primary and reflected sources. Table I lists each of these regions using the notation $\mathcal{R}^n$ for the nth region that is used for the rest of the paper, the conditions on the angular coordinates as measured from each of the edges, which pressure fields are present in this region, and a description of where the region exists in relation to the barrier. These same regions are depicted graphically in Fig. 3 for convenience. Some overlap exists between $\mathcal{R}^{III}$, $\mathcal{R}^{IV}$, and $\mathcal{R}^V$ since these only depend on their relevant angular coordinates. This overlap corresponds to diffraction at the barrier corner points, and it is assumed that the total pressure in these regions is formed by summing the pressure contributions from each edge region. More complicated effects are likely present at the corner points that are not accounted for in the current framework, such as those included in the boundary element method approach used by Yanpeng *et al.* (2018). For the purposes of this analysis, the receiver is assumed to be far away from the corner points, so these effects should be minor. If future work requires more accurate pressure calculations near the corners, analytic corner point diffraction models should be incorporated and the number of regions expanded accordingly. Additionally, in the previous discussion, the pressure contribution from each side of the barrier is computed using the expressions for an infinite edge. The work of Nikolaou and Menounou (2024) presents an integral expression for the diffracted field from a finite edge as the Fourier transform of the time-domain signaled obtained by integrating the re-radiated field over the length of the edge. Although there are differences between diffracted fields computed using expressions for diffraction across finite or the infinite edges, for the applications in this paper, these differences are assumed to be minor and the infinite expressions are maintained.

Despite these approximations, the rest of the analysis in this paper is general enough that for an analytic model of the pressure field, adapting this structure to more specific expressions required for a given application of interest should be straightforward.

C. Extended sources

The diffraction problem as constructed previously is for a single monopole; the next step is to extend to multiple sources. Assuming perfect coherence, the diffracted pressure fields can be computed for each source individually, and then the pressures summed linearly. A key consideration with this approach is that each of the five regions is dependent on the geometry of the radiating source. Each source has its own set of five regions, labeled $\mathcal{R}_i^n$, as in Fig. 3, which means field locations around the barrier may exist in different source regions, and the total pressure field at a given point may contain different contributions from each source. It is noted that the total pressure field generated by a single source is continuous. Although the geometric pressure field has a discontinuity across each shadow boundary where the direct, reflected, or transmitted fields start of stop existing, the diffracted pressure field has a similar, but opposite discontinuity at these same spatial locations such that the overall pressure field is continuous (Menounou and Asimakopoulos, 2021). When an extended source is modeled as a collection of point sources, the pressure field from each source is individually continuous, resulting in an overall pressure field that is also continuous.

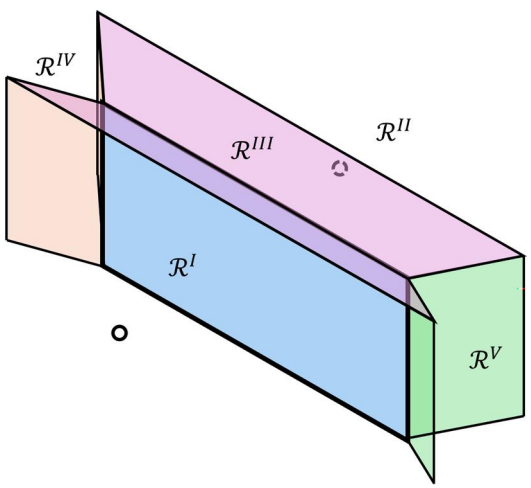

FIG. 3. The five regions around the barrier accompanying Table I. The two circles indicate the location of the primary (solid) and reflected (dashed) sources.

22 November 2026 18:10:11

The general acoustic radiation problem can be cast as $\boldsymbol{p} = \boldsymbol{Z}\boldsymbol{q}$ where $\boldsymbol{p} \in \mathbb{C}^{N\times 1}$ is the vector of pressures at N field locations $\left\{\boldsymbol{r}_i^f\right\}_{i=1}^{N}$, $\boldsymbol{q} \in \mathbb{C}^{M\times 1}$ is the vector of volume velocity source strengths at M source locations $\{\boldsymbol{r}_i^s\}_{i=1}^{M}$, and $\boldsymbol{Z} \in \mathbb{C}^{N\times M}$ is the transfer matrix that converts from $\boldsymbol{q}$ to $\boldsymbol{p}$, all of which are frequency-dependent, time-averaged quantities. The form of $\boldsymbol{Z}$ is dependent on the source and field geometry and includes field effects, such as a net flow or obstruction. When multiple effects are present, such as the presence of a ground reflection, $\boldsymbol{Z}$ can be decomposed into individual components, assuming that the effects combine linearly. For the current application, Table I lists six individual pressure fields; thus, the relevant transfer matrix is built from six components.

The free-field or primary pressure field, $\boldsymbol{p}^p$, is the simplest as the transfer function is just the free-field Green's matrix: $\boldsymbol{Z}_{ij}^p = (j\rho ck/4\pi|\boldsymbol{r}_i^f - \boldsymbol{r}_j^s|)e^{jk|\boldsymbol{r}_i^f - \boldsymbol{r}_j^s|}$ where $|\boldsymbol{r}_i^f - \boldsymbol{r}_j^s|$ is the distance between the ith field location and the jth source. The reflected pressure field, $\boldsymbol{p}^r$, can also be constructed in terms of a free-field Green's matrix using a source description reflected across the barrier: $\boldsymbol{Z}_{ij}^r = (j\rho ck/4\pi|\boldsymbol{r}_i^f - \boldsymbol{r}_j^s|)e^{jk|\boldsymbol{r}_i^f - \boldsymbol{r}_j^r|}$ where $|\boldsymbol{r}_i^f - \boldsymbol{r}_j^r|$ is the distance between the ith field location and the jth reflected source. Since this matrix acts on the reflected sources, the reflected pressure is defined as $\boldsymbol{p}^r = \boldsymbol{Z}^r\boldsymbol{q}^r$. By the method of images (Kinsler *et al.*, 1999), the reflected source strength is set as $\boldsymbol{q}^r = \boldsymbol{R}(\boldsymbol{\theta}^r)\boldsymbol{q}$ and the reflected pressure field is $\boldsymbol{p}_i^r = (\boldsymbol{Z}^r \circ \boldsymbol{R}(\boldsymbol{\theta}^r))\boldsymbol{q}_j$, where $\circ$ is the Hadamard product (element-wise multiplication), $\boldsymbol{R}(\boldsymbol{\theta}^r)$ is a matrix of pressure reflection coefficients from Eq. (2a), and $\boldsymbol{\theta}_{ij}^r$ is the specular reflection angle between the ith field points and the jth source. The reflected transfer function is then $\boldsymbol{Z}^r \rightarrow \boldsymbol{Z}^r \circ \boldsymbol{R}(\boldsymbol{\theta}^r)$. The transmitted pressure, $\boldsymbol{p}^t$, is similarly an extension of the free-field case; the only difference is that for field locations beyond the wall, the pressure must be scaled by the appropriate pressure transmission coefficient, thus $\boldsymbol{Z}^t = \boldsymbol{Z}^p \circ \boldsymbol{T}(\boldsymbol{\theta}^t)$ where $\boldsymbol{\theta}_{ij}^t$ is the transmission angle between the ith field points and the jth source. For the three diffracted fields, Eq. (5) defines the appropriate transfer function. However, to account for the boundary's finite impedance, both components of the diffracted transfer function are considered individually. The first term, $\boldsymbol{Z}^{d,p}$ acts on the primary sources, while the second term, $\boldsymbol{Z}^{d,r}$ acts on the reflected sources. In this form, the diffracted pressure field is calculated as $\boldsymbol{p}^d = \boldsymbol{Z}^{d,p}\boldsymbol{q} + \boldsymbol{Z}^{d,r}\boldsymbol{q}^r$. As with the reflected field, let $\boldsymbol{q}^r = \boldsymbol{R}(\boldsymbol{\theta}^r)\boldsymbol{q}$ and substitution yields $\boldsymbol{p}^d = \left(\boldsymbol{Z}^{d,p} + \boldsymbol{Z}^{d,r} \circ \boldsymbol{R}(\boldsymbol{\theta}^r)\right)\boldsymbol{q}$. The transfer function for the diffracted field is then $\boldsymbol{Z}^d \rightarrow \boldsymbol{Z}^{d,p} + \boldsymbol{Z}^{d,r} \circ \boldsymbol{R}(\boldsymbol{\theta}^r)$ for $d \in \{\text{Top}, \text{Left}, \text{Right}\}$.

As noted previously, the regions surrounding the barrier (see Fig. 3) define which pressure fields are present and where (see Table I). As such, each region will have its own composite matrix depending on the contributing fields. Explicitly, these are $\boldsymbol{Z}^I = \boldsymbol{Z}^p + \boldsymbol{Z}^r + \boldsymbol{Z}^{\text{Top}} + \boldsymbol{Z}^{\text{Left}} + \boldsymbol{Z}^{\text{Right}}$ for $\mathcal{R}^I$ (in front of the barrier), $\boldsymbol{Z}^{II} = \boldsymbol{Z}^t + \boldsymbol{Z}^{\text{Top}} + \boldsymbol{Z}^{\text{Left}} + \boldsymbol{Z}^{\text{Right}}$ for $\mathcal{R}^{II}$ (behind the barrier), $\boldsymbol{Z}^{III} = \boldsymbol{Z}^p + \boldsymbol{Z}^{\text{Top}}$ for $\mathcal{R}^{III}$ (above the barrier), $\boldsymbol{Z}^{IV} = \boldsymbol{Z}^p + \boldsymbol{Z}^{\text{Left}}$ for $\mathcal{R}^{IV}$ (left of the barrier), and $\boldsymbol{Z}^V = \boldsymbol{Z}^p + \boldsymbol{Z}^{\text{Right}}$ for $\mathcal{R}^V$ (right of the barrier). Since each composite transfer function acts on the vector of source strengths and returns the pressure at all field locations, these need to be masked according to the appropriate spatial domain. A masking operator is now defined as $\boldsymbol{\mathcal{B}}_{ij}^n = 1$ when $\boldsymbol{r}_i^f \in \mathcal{R}_j^n$ and 0 otherwise, i.e., whether the ith field point is within $\mathcal{R}^n$ as cast by the jth source. The masked matrices are then computed as $\boldsymbol{\mathcal{Z}}^n = \boldsymbol{Z}^n \circ \boldsymbol{\mathcal{B}}^n$. Now, each composite transfer function effectively singles out a region around the barrier and computes the appropriate pressure fields within that region. Since the radiation within each region is independent of the others, linearity can be applied to compute a total transfer function: $\boldsymbol{\mathcal{Z}} = \boldsymbol{\mathcal{Z}}^I + \boldsymbol{\mathcal{Z}}^{II} + \boldsymbol{\mathcal{Z}}^{III} + \boldsymbol{\mathcal{Z}}^{IV} + \boldsymbol{\mathcal{Z}}^V$ and the pressure surrounding the barrier is computed as $\boldsymbol{p} = \boldsymbol{\mathcal{Z}}\boldsymbol{q}$.

D. Cross-spectral formulation

The previous development assumes that the sources are perfectly coherent. A natural extension is to consider what happens when the radiated fields do not fully interact, that is, when the sources are partially coherent, which is an important aspect in several areas of aeroacoustics, including supersonic jet noise (Mathews and Gee, 2024; Papamoschou, 2011). Making this extension requires recasting the problem in terms of cross-spectral matrices (CSM) CSMs (see Olaveson and Gee, 2026). The CSM is defined as $\boldsymbol{C} = \langle \boldsymbol{p}\boldsymbol{p}^* \rangle$, where $\langle\cdot\rangle$ is the expectation value and $\cdot^*$ is the complex conjugate. The expectation value is assumed to act across discrete time blocks when the time series are converted to spectra. In this sense, the cross-spectral matrix cannot be obtained given the pressure vectors alone unless the linear coherence, $|\gamma|$, between each pair of field locations is known, in which case $\boldsymbol{C}_{ij} = \boldsymbol{p}_i\boldsymbol{p}_j^*|\gamma_{ij}|$. Using the transfer matrix $\boldsymbol{Z}$, the CSM is computed as

$$\boldsymbol{C} = \langle \boldsymbol{p}\boldsymbol{p}^H \rangle, \tag{6}$$

$$= \langle \boldsymbol{Z}\boldsymbol{q}\boldsymbol{q}^H\boldsymbol{Z}^H \rangle, \tag{7}$$

$$= \boldsymbol{Z}\boldsymbol{S}\boldsymbol{Z}^H, \tag{8}$$

where $\boldsymbol{S} = \langle \boldsymbol{q}\boldsymbol{q}^* \rangle$ is the source cross-spectral matrix (SCSM) and $\cdot^H$ is the Hermitian transpose. As with $\boldsymbol{C}$, the SCSM is not directly obtained from a vector of source strengths, but rather, it must be obtained in other ways, such as through cross-spectral beamforming methods like hybrid beamforming (HM) (Padois *et al.*, 2014; see also Harker *et al.*, 2019 and Olaveson and Gee, 2025 for application to a supersonic jet). The advantage of this type of model is that partial coherence and phase relationships are expressed directly in the source description, allowing for more complicated arrangements and interactions. Under this construction and the previous development, the cross-spectral matrix

22 November 2026 18:10:11

https://doi.org/10.1121/10.0047519

describing the pressure in the field, including the effects of the barrier, is computed using Eq. (8): $\boldsymbol{C} = \boldsymbol{\mathcal{Z}}\boldsymbol{S}\boldsymbol{\mathcal{Z}}^{H}$.

Up to this point, ground reflections have been ignored. In free-field applications, reflections off a rigid ground can be handled by simulating an image source. However, in the presence of a barrier, a simple image source is not sufficient. For a receiver on the other side of the barrier and to first order, there are four diffraction paths around each edge: regular diffraction, ground reflection before diffraction, ground reflection after diffraction, and a ground reflection before and after diffraction. The first path is the formulation discussed previously; each of the other paths is computed by repeating this analysis but using combinations of a ground-reflected source description and a ground-reflected version of the barrier.

III. APPLICATION

With the theoretical development complete, the framework is now applied to a barrier problem for jet noise reduction. For application on an aircraft carrier, there is a desire to make a barrier highly mobile and potentially transparent. It has been proposed that a curtain of water might be an option (Office of Naval Research, 2025). Furthermore, injecting bubbles into a water curtain may provide further noise reduction. In underwater acoustics, bubbles have been shown to be effective at controlling noise fields in applications ranging from offshore windmill construction (Bohne *et al.*, 2019) to WWII battleship stealth (Domenico, 1982). Given their success in underwater noise control, the potential of a curtain of bubbly water to reduce jet noise has resulted in a number of recent papers and presentations investigating this possibility (see Olaveson *et al.*, 2025; Mankbadi and Uribe, 2025; and Patel and Viswanath, 2026). In this section, full-scale jet noise data are used to construct an acoustically equivalent cross-spectral noise source. An example problem is then defined by placing an observer at a realistic location near the aircraft behind a thin layer of water with injected bubbles. To identify the effects of bubbles, the IL of the barrier is computed and compared to a barrier of pure water. Last, the barrier is modeled as an anechoic surface to represent the best-case scenario for this arrangement, and implications are discussed.

A. Experiment

The application in this paper uses noise data collected near the T-7A jet. This same dataset has been used repeatedly in jet noise source analyses (Mathews and Gee, 2024; Gee *et al.*, 2025; Olaveson and Gee, 2024). While only a summary of the relevant details is provided here, a full description of the measurement can be found in Leete *et al.* (2021).

Noise data were collected in the early morning of August 18, 2019, at Holloman Air Force Base in New Mexico. The experiment consisted of an F404 engine installed on a T-7A trainer aircraft tied to the runway and oriented with the nose towards the jet blast deflector to preserve the full extent of the plume. The engine was cycled through six engine conditions ranging from idle to military power (MIL) and afterburner (AB) conditions. Each condition was held long enough to record a minimum of 30 s of steady-state acoustic data before continuing. Each runup from idle to AB was repeated six times for broader averaging. Although the full measurement included over 200 microphones sampling the acoustic near and far fields, the analysis in this paper only uses a portion of the near-field measurements as sampled by an array of 120 ground-based microphones. This array (depicted in Fig. 4) is referred to as the "imaging array" and is comprised of GRAS 46BD and 46BG 1/4″ pressure microphones. The microphone sampling rate was set to 204.8 kHz in anticipation of the phased array analyses and shock characterization. The array began a few meters forward of the aircraft and ran parallel to the jet centerline before angling outward along the approximate shear layer (∼8°). The inter-microphone spacing was varied across the array in anticipation of the expected noise features present at each portion of the array. A smaller spacing was used to the sideline where higher frequency noise is expected to dominate, and a larger spacing downstream where low-frequency radiation is prevalent. A set of sample angles are shown relative to the microphone array reference point (MARP) to demonstrate the angular span of the array.

An important result from a previous analysis (Olaveson and Gee, 2025) is the construction of an acoustic ESM. Since providing an in-depth discussion on the requisite methods would detract from the purpose of this paper, a simple description of the process will be provided here with further details reserved elsewhere (Harker *et al.*, 2019; Olaveson and Gee, 2025; Padois *et al.*, 2014). Once data at the imaging array are collected, the recordings are compiled into CSMs. These matrices contain the pressure amplitudes and phase relationships between each measurement location for a given frequency. From the measured CSM, the HM method (Padois *et al.*, 2014) uses a cross-spectral minimization approach to determine the SCSM for a prescribed set of source locations. The result is a collection of monopoles with amplitude and phase relationships that best describe the acoustic pressures when radiated out to the measurement array. Since the ESM describes the properties of an acoustically equivalent source, it can also be used to compute the

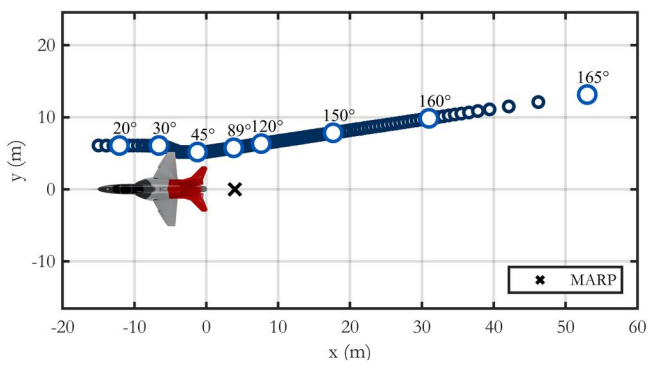

FIG. 4. Schematic of the T-7A near-field imaging array microphone setup.

22 November 2026 18:10:11

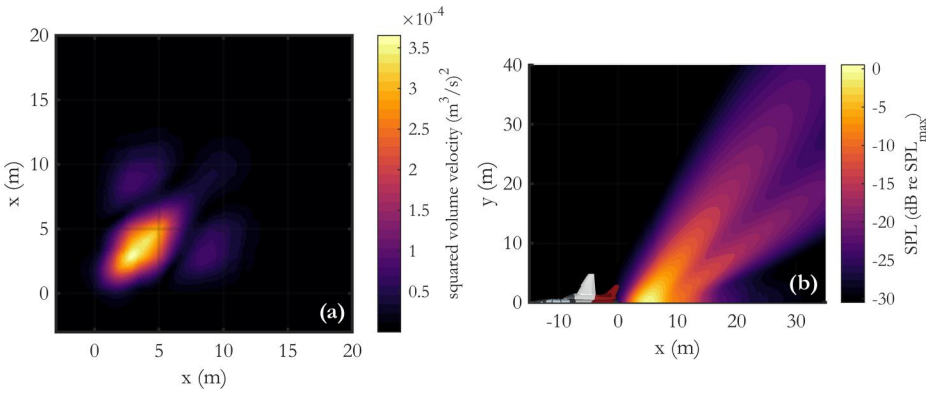

FIG. 5. Sample source CSM (a) and the radiated field (b) at 201 Hz and MIL.

pressure field at locations other than those measured by the experiment. An example of a computed ESM at MIL is given in Fig. 5, with cross-spectral source strengths in Fig. 5(a) and the corresponding field reconstruction in 5b at 201 Hz, which is a peak frequency. In Fig. 5(a), the main diagonal gives the squared source amplitude. Off-diagonal elements indicate the presence of coherence between sources, which is important for field radiation properties (Mathews and Gee, 2024), and other noise metrics such as sound power (Olaveson and Gee, 2026). The associated total-field reconstruction is shown in Fig. 5(b) and demonstrates the multi-lobed behavior that is prevalent on full-scale military jets, but largely absent at lab-scale with a few exceptions (Kumar *et al.*, 2025). While the spatiospectral lobe phenomenon is not important to the results of this paper, it is important that the HM-educed ESM replicates the sound field produced by a full-scale military jet, including coherence properties, which was demonstrated by Harker *et al.* (2019).

B. Application

Using the T-7A noise source model, the potential noise reduction of a curtain of bubbly water can be explored. According to Aubert and McKinley (2011), the final checker is closest to the aircraft during takeoff from an aircraft carrier and stands about 9 meters to the sideline and aligned with the nozzle. Assuming they stand about 2 meters tall, the observer is located at $(0, 9, 2)$ in the coordinate system with origin on the ground directly beneath the nozzle. Between the observer and the jet is a one centimeter-thick, five-by-five meter layer of water containing bubbles as depicted in Fig. 6, which satisfies the $kL \gg 1$ requirement noted in Eq. (4) for all sources in the ESM. While the exact mechanical design of the curtain is not considered here, it is assumed to be produced by an elevated structure with bubble-injected water falling in such a way as to produce a uniform barrier. In this analysis, the ground is assumed to be rigid. The same process has been performed using an absorptive ground and the results are qualitatively similar, just at a lower sound pressure level (SPL), higher insertion loss (IL), and without the ground reflection nulls.

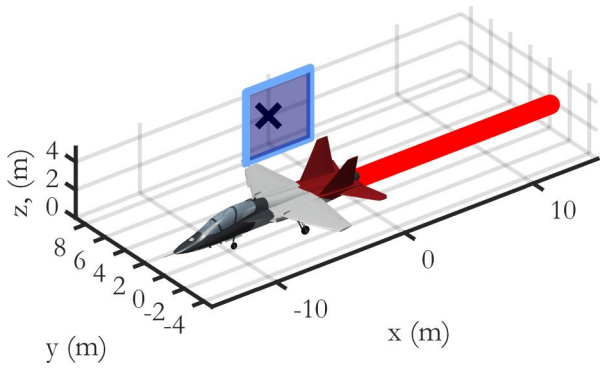

FIG. 6. Application setup. The bubbly curtain is shown in blue, the red circles mark source locations of the T-7A ESM, and the black x is the position of the observer over a rigid ground. Included is a to-scale model of the T-7A.

Since the presence of bubbles within the curtain fundamentally changes the acoustic properties of the barrier, defining a single wavenumber to describe propagation through the bubbly fluid requires an equivalent medium theory. Fortunately, with so many underwater applications of bubble swarms, this is a problem that has been addressed in the literature. This paper uses the results from Caflisch *et al.* (1985), who provided physical justification for the effective equations presented by Van Wijngaarden (1968, 1972). Their work showed that the effective sound speed within a bubbly fluid can be computed by adding a correcting term to the pure sound speed as

$$\frac{1}{(c^m)^2} = \left(\frac{k^m}{\omega}\right)^2 = \frac{1}{(c^0)^2} + \frac{3\beta}{a^2(\omega_0^2 - \omega^2)}, \tag{9}$$

where c^m is the speed of sound in the composite medium, c^0 is the sound speed in the pure fluid, a is the bubble radius at rest, $\beta = (4/3)\pi a^3 n$ is the void fraction, $n(a)$ is the density of bubbles of radius a, and ω_0 is the natural or Minnaert (1933) frequency of the bubble. While this expression is for a monodisperse bubble population, the effect of adding more bubbles is cumulative. By iteratively making the update $c^m \to c^0$ and integrating over a distribution of bubble radii, the effective wavenumber becomes

$$(k^m)^2 = \left(\frac{\omega}{c^0}\right)^2 + 4\pi\omega^2 \int \frac{an(a)}{\omega_0^2(a) - \omega^2 + 2jb\omega} da, \tag{10}$$

22 November 2026 18:10:11

https://doi.org/10.1121/10.0047519

where now $\omega_0(a)$ is expressed as a function of bubble radius and b is an additional damping factor that accounts for viscous, thermal, and acoustic losses. While damping effects are ignored in the Caflisch *et al.* (1985) derivation, the form of the coefficients is provided by Prosperetti (1977). This wavenumber now describes how an acoustic wave propagates through the bubbly fluid and can be substituted into Eq. (2) to solve the reflection and transmission coefficients for a given $n(a)$. One of the benefits of this expression is that there is no need to track the spatial distribution of bubbles, just the density of bubbles at each radius. This expression is valid for linear waves and assumes that the void fraction is small enough that the bubbles are non-interacting, about 1%. The effective density is $\rho^m = (1-\beta)\rho^0 + \beta\rho^a$, where ρ^0 is the density of the pure fluid and ρ^a is the density of air.

For application to the bubbly curtain, there are a few practical constraints to consider. First, the T-7A jet noise radiation peaks in the range of 200–500 Hz (Leete *et al.*, 2021). Second, the curtain is assumed to be produced by water falling from an elevated structure with bubbles injected at the top. In application, this curtain must be relatively thin, about 1 cm seems to be what is physically practical. The first condition places the desired range of bubble radii between about 6 mm and 2 cm. However, the second condition suggests that only bubbles smaller than this range can fit within a realistic curtain. The compromise is to define a bubble distribution that targets as many low frequencies as possible, while fitting within the curtain. A distribution is desired since it has been shown that a bubble swarm can have an "effective" bubble radius that attenuates frequencies lower than the resonance frequencies of the contributing bubbles (Doheny, 2024). To extend the effective bandwidth while enforcing that there are no large bubbles, a lognormal distribution is used

$$n(a) = \frac{N_0}{a\sqrt{2\pi\sigma^2}} e^{-(\ln a - \ln \overline{a})^2/2\sigma^2}, \tag{11}$$

where $N_0 = 1.3 \times 10^5$ bubbles/m^3 is the overall bubble density set so that the void fraction $\beta = \int (4/3)\pi a^3 n(a) da \approx 1\%$, $\sigma = 0.2$ is the logarithmic standard deviation, and $\overline{a} = 2.5$ mm is the geometric mean bubble radius. These parameters were chosen to allow for as many large bubbles as possible, while restricting their sizes to within the curtain. The bubble density distribution is plotted in Fig. 7(a). Since $n(a)$ is a density distribution, the curve in Fig. 7(a) cannot be interpreted as a density of bubbles at a given radius. Rather, to determine a specific bubble density, $n(a)$ must be integrated across a range of bubble radii, with the total number of bubbles per cubic meter given as $\int_0^\infty n(a)da = N_0$. The full-width, half-maximum of this distribution covers a range of bubble radii between about 1.9 and 3.0 mm corresponding to resonance frequencies ($f_0 = \omega_0/2\pi$) between 1100 and 1700 Hz with a peak at 1300 Hz. While these frequencies do not cover the standard peak frequencies of full-scale military aircraft, including larger bubbles becomes impossible as they physically cannot fit within the curtain constraints as presented. The pressure reflection and transmission coefficients are solved using Eqs. (2) and (10) at a range of angles and frequencies and plotted in Figs. 7(b) and 7(c). While these maps are not visually interesting, the resonance effects of the bubble distribution occur near 1000 Hz where the bubbly fluid absorbs a portion of the incident energy, leading to cases where $|T|^2 + |R|^2 < 1$. Despite this, the coefficients are remarkably uniform, except at grazing incidence.

In application, such a bubbly curtain would likely require water falling from some elevated structure or some other flow. However, for the purposes of this analysis, the barrier is assumed to be stationary, which is valid to first order since the acoustic wave speed is much faster than the velocity of the falling water and the aggregate effect of the flow represents a minimal path deflection across small distances. Similarly, bubbles within the fluid can be assumed to be stationary.

C. Insertion loss

Using the described barrier geometry and composition in conjunction with the HM-computed ESMs at MIL, the SPL at the receiver is computed with and without the bubbly curtain and plotted in Fig. 8(a). The orange curve shows the predicted SPL without the presence of the barrier and contains spectral dips near 250 and 600 Hz that correspond to reflections from the rigid ground. The blue curve shows the SPL in the presence of the bubbly curtain and notably lacks the same ground reflection structure. The barrier IL is taken as the difference between the two curves and is plotted in Fig. 8(b). From this curve, it is seen that the bubbly curtain can reduce the radiated noise by around 5 dB at frequencies below about 200 Hz. At higher frequencies, the insertion loss increases, though ground reflections from the free-field

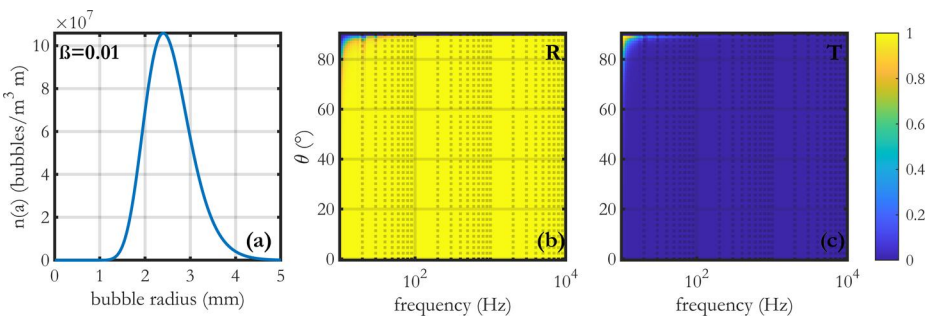

FIG. 7. Sample bubble density distribution (a) and the corresponding pressure reflection (b) and transmission (c) coefficients as a function of frequency and angle.

22 November 2026 18:10:11

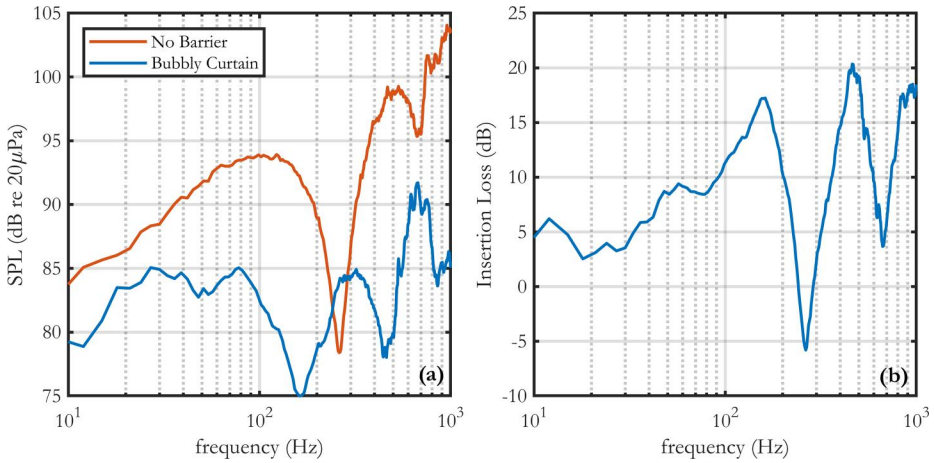

FIG. 8. The predicted sound pressure levels at the receiver location with and without the bubble curtain (a) and the insertion loss (b).

case cause some additional spiking. The increased insertion loss is explained by the shifting directivity of the noise source. As frequency increases, the noise source location moves upstream towards the observer and the radiation angle moves towards the sideline (Olaveson *et al.*, 2022). Although the primary radiation lobe is never directly incident on the curtain, the increased levels near the curtain are attenuated.

While placing a bubbly curtain between the jet and the receiver reduces the predicted noise, a relevant question is "how important are bubbles?". To address this, the same scenario is evaluated assuming no bubbles in the curtain. As before, the IL is computed, but this time, the difference between the water IL and the bubble IL is plotted in Fig. 9. From this figure, the difference between a curtain of bubbly water and a curtain of pure water is less than 0.05 dB, which is negligible. This is likely due to the decreased mass of the curtain by including bubbles. With a lower density curtain, more acoustic energy travels through the curtain and the bubbles are unable to reduce the additional noise at these frequencies. Regardless, the performance relative to water is so minute that including bubbles in the curtain does not significantly change the insertion loss.

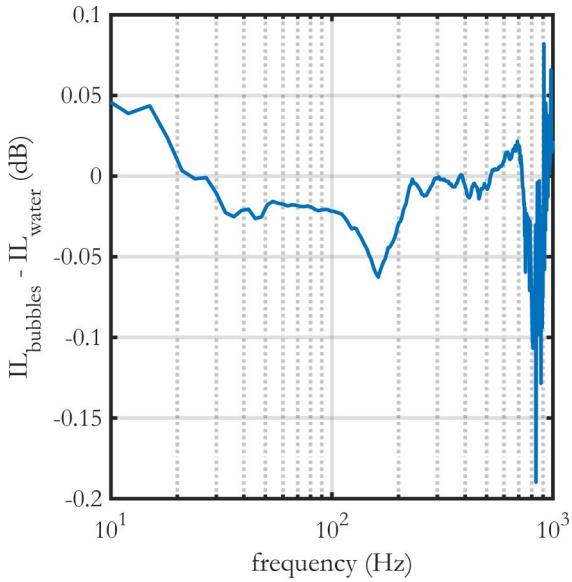

FIG. 9. The insertion loss of a bubbly curtain relative to that of a curtain of pure water.

The result that bubbles make a negligible difference to the overall IL is dependent on the defined bubble distribution, and it is likely that a bubble distribution exists that produces more IL than this scenario. While a parameter optimization is not attempted here, a best-case scenario can be tested under the current framework by replacing the water curtain with an anechoic barrier. The curtain is approximated as anechoic by setting the reflection and transmission coefficients to zero, $R = T = 0$, for all frequencies and angles, meaning that the barrier absorbs any incident energy and only diffraction contributes to the pressure field measured behind the barrier. While such a structure may not be mechanically feasible, this computation represents an optimal scenario for this barrier geometry. The curtain IL is calculated under these new conditions and compared to the pure water case. The two IL spectra are shown in Fig. 10(a) and their difference in Fig. 10(b). As expected, an anechoic barrier performs better than a pure water curtain, particularly at low frequencies, where the IL is between 10 and 15 dB. At higher frequencies, the difference between the two becomes less distinct. Between 200 and 300 Hz, the anechoic barrier underperforms relative to water. The exact reason for this result is unclear, but it may be related to interference phenomena caused by interactions with the barrier that are not present in the anechoic case and suggests that a truly optimal curtain will need to take advantage of these barrier interactions.

The analysis in this section provides two key conclusions. First, bubbles make a negligible difference in terms of water barriers for jet noise control, as implemented by this model. The primary reason is due to the practical constraints placed on creating a water curtain. Without a thicker curtain, bubble radii are limited and resonances cannot be sufficiently tuned to target peak jet noise frequencies. However, even under an optimized design, bubbles in a curtain of water are fundamentally different from bubbly layers in underwater applications. When bubbly layers are used to control underwater noise sources, absorption dominates

22 November 2026 18:10:11

https://doi.org/10.1121/10.0047519

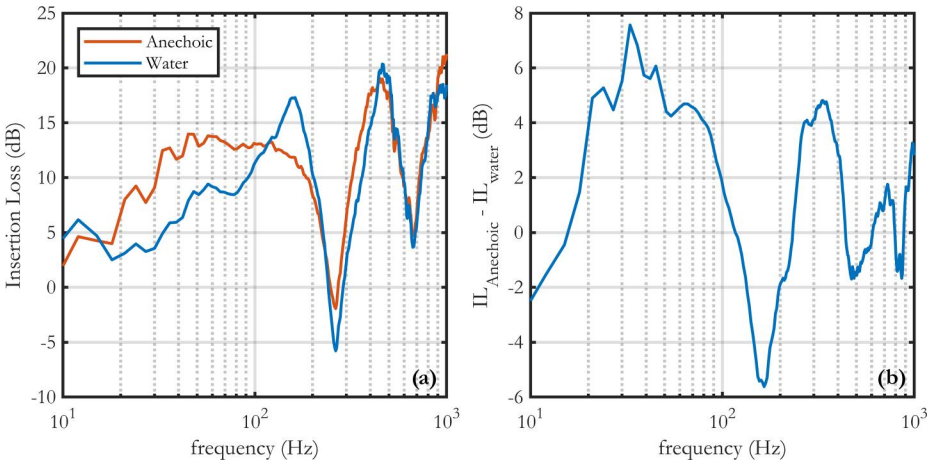

FIG. 10. The insertion loss of an anechoic barrier compared to a barrier of pure water. Note that the water insertion loss is nearly identical to the curve in Fig. 8.

because most of the energy is transmitted into the layer. On the contrary, for application to jet noise, the large impedance mismatch between the air-water interfaces means that most of the incident energy is reflected and relatively little enters the curtain to be absorbed by the bubbles. Although this conclusion is reached using a small void fraction bubble model (Caflisch *et al.*, 1985), it may not be unique to this equivalent medium theory. Other models that can allow for a larger void fraction or higher-order bubble interactions would likely suffer from the same domain mismatch, unless they allowed for more energy to enter the barrier, which begins to approach the anechoic surface example where all the energy is absorbed by the barrier.

The second key conclusion is that jet noise reduction using a barrier is fundamentally a diffraction problem. When a source and receiver are separated by a barrier, there are 13 total paths describing the acoustic field, one through the barrier and twelve diffraction paths including ground reflections. Transmission through the barrier is the dominant noise path, and if a hole were present in the barrier, diffracted paths would be inconsequential. However, when the transmission is perfectly controlled, as with the anechoic barrier, those same diffracted paths dominate, and any extra noise reduction within the barrier is outclassed. Similar conclusions were observed by Patel and Viswanath (2026), who developed a preliminary numerical scheme to determine the effect of a 2D water barrier in the presence of a monopole.

D. Partial coherence

The partially coherent nature of the jet noise source has been repeatedly emphasized in this paper as an important component of the diffracted noise field, but the effect of neglecting coherence has not been discussed. To demonstrate the importance of including partially coherent interactions, the same bubbly curtain diffraction analysis is completed using fully coherent and incoherent source models. For each case, a cross-spectral matrix is constructed using the expression $\boldsymbol{C}_{ij} = \boldsymbol{p}_i \boldsymbol{p}_j^* |\gamma_{ij}|$ and setting the coherence to either one or zero. The original phase relationships from the HM model are preserved in the fully coherent model but are lost in the incoherent model since the cross-terms go to zero. The corresponding field radiation is then computed at 201 Hz and plotted in Fig. 11 for the fully coherent model [Fig. 11(a)], the original HM model [Fig. 11(b)], and the incoherent model [Fig. 11(c)]. Included in each subfigure is the location of the water curtain in blue and the observer in red for reference, though diffraction calculations have been neglected in this reconstruction to illustrate the effect of coherence on field radiation. From these figures, it is shown that the noise source directivity is described primarily by the source phase relationship. The incoherent model [Fig. 11(c)] has no phase relationship and, as such, produces a somewhat omnidirectional sound field. The coherent model [Fig. 11(a)] has all the phase relationships from the original HM model and exhibits the same multi-lobed behavior but includes additional lobes in the forward direction. These extraneous lobes are not present in the HM model because the partial coherence restricts which sources couple, resulting only in the measured radiation lobes. The maximum SPL ($\mathrm{SPL}_{\mathrm{max}}$) from each source description is included in the top left corner of each subfigure. The coherent model has the highest $\mathrm{SPL}_{\mathrm{max}}$, which is to be expected since coherent interactions can interfere constructively and boost the levels, while the incoherent model has the lowest $\mathrm{SPL}_{\mathrm{max}}$ because the acoustic fields radiated by those sources are non-interacting.

Using each of these source models, the diffracted pressure field is computed in the vicinity of the bubbly curtain as in Fig. 8, and the sound pressure level spectra are plotted together in Fig. 12(a) and the corresponding IL curves in Fig. 12(b). The diffracted pressure field from the incoherent model generally has a higher amplitude than the partially coherent model, and the fully coherent model is the most erratic. Since the incoherent model has the lowest $\mathrm{SPL}_{\mathrm{max}}$, it is initially surprising that this model has the largest diffracted pressure field. This result is explained by the source directivities. The field radiation from the incoherent source model [Fig. 11(c)] is largely omnidirectional and has an amplitude of about 105 dB at the curtain; on the contrary, both the coherent [Fig. 11(a)] and partially coherent [Fig. 11(b)] models show amplitudes less than 100 dB. This

22 November 2026 18:10:11

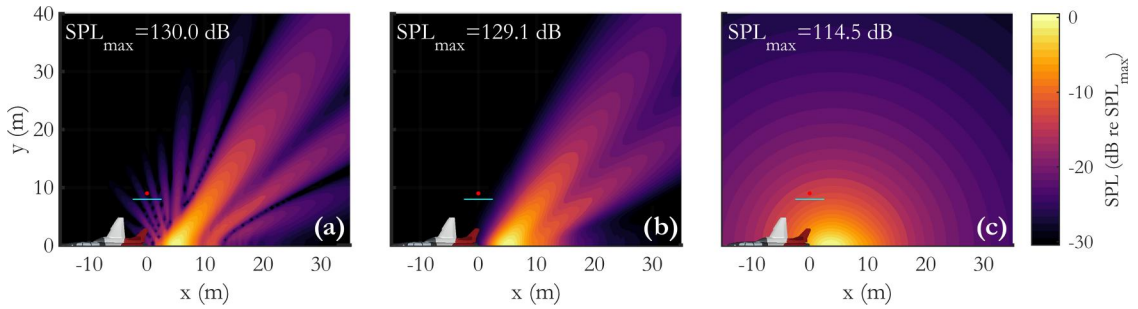

FIG. 11. Sample field reconstructions using a fully coherent model (a), the partially coherent HM model (b), and a fully incoherent model (c).

same trend continues through frequency until about 500 Hz, at which point the directivity from the HM model increases the levels at the curtain above the incoherent model. The erratic behavior from the fully coherent model is described by the extraneous radiation lobes in the forward direction. Since this source model is fully coherent, it exhibits a strong interference pattern in the forward direction. As frequency increases, these lobes evolve, resulting in alternative constructive/destructive interference on the barrier. For the IL in Fig. 12(b), each curve follows roughly the same trend as the HM model, which is the same as in Fig. 8. The perfectly coherent model exhibits the same spikiness as before. The incoherent model is largely similar to the HM model, including the sharp dip near 300 Hz caused by the coherent ground reflection null in the reference spectrum, despite the incoherent nature of the source itself.

IV. CONCLUSION

This paper has presented a framework for determining the pressure field radiated from an extended, partially coherent noise source in the presence of a finite barrier of arbitrary impedance. The standard three-layer analysis from Kinsler *et al.* (1999) is combined with analytic expressions for the diffracted pressure around a semi-infinite barrier (Menounou *et al.*, 2000). Multiple edges are handled by assuming linearity in the diffracted pressure fields and defining the relevant regions of existence. The arbitrary impedance of the curtain is handled by determining appropriate reflection and transmission coefficients and scaling the diffracted pressure field accordingly. The problem is then cast into a cross-spectral formulation by defining transfer matrices that act on a vector of source strengths and return the relevant pressure field. Individual transfer matrices are combined and masked based on where each field is present.

For application, several projects funded by the Office of Naval Research (ONR) are interested in the possibility of a curtain of bubbly water as a noise reduction mechanism (see Olaveson *et al.*, 2025; Patel and Viswanath, 2026; Mankbadi and Uribe, 2025; and Office of Naval Research, 2025). To address this problem, the framework is applied to an example problem of an observer behind a curtain of bubbly water near a T-7A-installed F404 jet at the location of the final checker (Aubert and McKinley, 2011). The analysis uses a previously constructed, partially coherent ESM of the jet to compute the insertion loss of a bubbly curtain. To investigate the relevance of injected bubbles, the same scenario is again considered assuming a curtain of pure water. It is shown that for the proposed bubble distribution, the acoustic impact of bubbles is negligible. As an extreme case, the same comparison is also made by modeling the curtain as an anechoic surface. While this case improves the insertion loss at low frequencies, the improvement over pure water is only a few dB and approaches zero at high frequencies.

In the end, bubbly media are ill-suited for jet noise control, despite their success in underwater applications. The barrier problem, as discussed here, is diffraction-dominated.

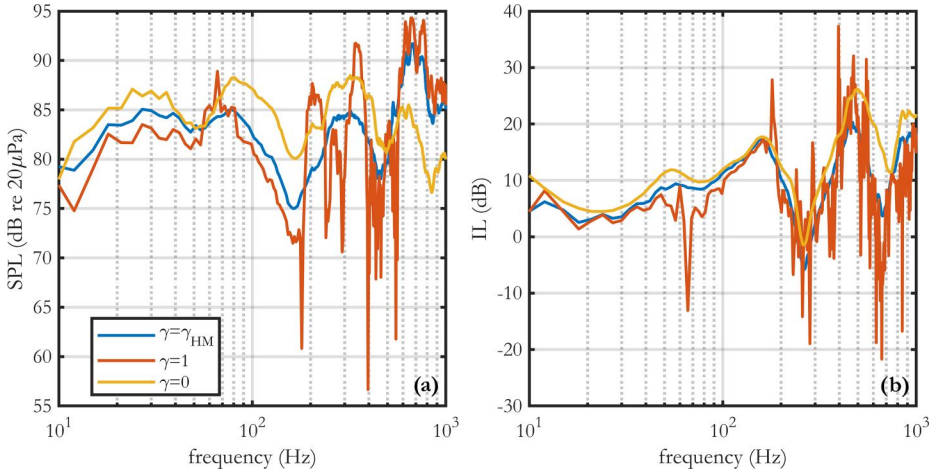

FIG. 12. (a) SPL predicted at the observer for the coherent, partially coherent, and incoherent source models, and (b) the insertion loss for the same cases. The blue curves ($\gamma = \gamma_{HM}$) are identical to the diffracted pressures in Fig. 8.

22 November 2026 18:10:11

While transmission through the barrier is a dominant path, there are twelve other paths diffracting around the barrier edges, and reducing the transmitted path cannot overcome the diffraction. Future work concerned with jet noise reduction via barriers should focus on reducing the diffracted noise field, perhaps by optimizing barrier geometry while maintaining a relatively large acoustic impedance.

While the framework developed here is a significant contribution to radiation from partially coherent noise sources, there are still some potential improvements that future work should consider. In this work, corner point diffraction was handled by superposing diffraction from each adjacent edge, and expressions for infinite edge diffraction were used to model a finite barrier. Whether or not these approximations are valid or if better models are warranted for this application is still an open question. The barrier was also assumed to be thin relative to a wavelength; however, thick barriers may be more effective at noise reduction, and thus double diffraction models should be considered. Last, this paper has treated the problem theoretically and numerically applied it to the jet noise problem, but experimental validation is still required. While the current ONR project funding this work has plans to validate the framework by repeating the experiment in Sec. III with Virginia Tech's afterburning jet (Kumar *et al.*, 2025), other validation work regarding the key components of the model should still be considered. These include experimentally quantifying the error associated with modeling finite-length diffraction using the expressions for an infinite barrier and designing experiments where the barrier impedance or source coherence can be modified. Results from these validations would provide valuable improvements to the formulation of the transfer functions that form the foundation of this framework.

ACKNOWLEDGMENTS

This work was funded by the Office of Naval Research and by the Utah Space Grant Fellowships.

AUTHOR DECLARATIONS

Conflict of Interest

The authors have no conflicts of interest to declare.

DATA AVAILABILITY

The data used in this analysis are available upon reasonable request from the T-7A program office.

Aubert, A., and McKinley, R. (**2011**). "Measurements of jet noise aboard US Navy aircraft carriers," in *Proceedings of the AIAA Centennial of Naval Aviation Forum*, Virginia Beach, VA, AIAA Paper No. 2011-6947.

Bohne, T., Grießmann, T., and Rolfes, R. (**2019**). "Modeling the noise mitigation of a bubble curtain," J. Acoust. Soc. Am. **146**, 2212–2223.

Bowman, J. J., Senior, T. B. A., and Uslenghi, P. L. E. (**1969**). *Electromagnetic and Acoustic Scattering by Simple Shapes* (North-Holland Publishing Company, Amsterdam).

Caflisch, R. E., Miksis, M. J., Papanicolaou, G. C., and Ting, L. (**1985**). "Effective equations for wave propagation in bubbly liquids," J. Fluid Mech. **153**, 259–273.

Corso, J. F. (**1963**). "Bone-conduction thresholds for sonic and ultrasonic frequencies," J. Acoust. Soc. Am **35**, 1738–1743.

Doheny, V. V. (**2024**). *Characterization of Targeted Microbubbles for Adhesiolysis* (Boston University, Boston).

Domenico, S. N. (**1982**). "Acoustic wave propagation in air-bubble curtain in water—Part 1: History and theory," Geophysics **47**(3), 345–353.

Gee, K. L., Olaveson, T. W., and Mathews, L. T. (**2025**). "Convective Mach Number and Full-Scale Supersonic Jet Noise Directivity," AIAA J. **63**(4), 1393–1404.

Harker, B. M., Gee, K. L., Neilsen, T. B., Wall, A. T., and James, M. M. (**2019**). "Source characterization of full-scale tactical jet noise from phased-array measurements," J. Acoust. Soc. Am. **146**, 665–680.

Henderson, B., and Bridges, J. (**2010**). "An MDOE Investigation of Chevrons for Supersonic Jet Noise Reduction," in *Proceedings of the 16th AIAA/CEAS Aeroacoustics Conference*, AIAA Paper No. 2010-3926.

Jacobsen, F. (**1989**). "Active and reactive, coherent and incoherent sound fields," J. Sound Vib **130**(3), 493–507.

Kinsler, L. E., Frey, A. R., Coppens, A. B., and Sanders, J. V. (**1999**). *Fundamentals of Acoustics*, 4th ed. (John Wiley & Sons, Inc., New York).

Kumar, A., Meadows, J., Olaveson, T. W., Gee, K. L., Mathews, L. T., and Pratt, H. J. (**2025**). "Far-field noise measurements of a supersonic jet operating near afterburning conditions," Aerosp. Sci. Technol. **157**, 109842.

Kurze, U. J. (**1974**). "Noise reduction by barriers," J. Acoust. Soc. Am. **55**, 504–518.

Lax, M., and Feshback, H. (**1948**). "Absorption and scattering for impedance boundary conditions on spheres and circular cylinders," J. Acoust. Soc. Am. **20**, 108–124.

Leete, K. M., Vaughn, A. B., Bassett, M. S., Rasband, R. D., Novakovich, D. J., Gee, K. L., Campbell, S. C., Mobley, F. S., and Wall, A. T. (**2021**). "Jet Noise Measurements of an Installed GE F404 Engine," in *Proceedings of the AIAA SciTech Forum*, Virtual Event.

Li, J.-F., Pascal, J.-C., and Carles, C. (**1998**). "Energy fields of partially coherent sources," J. Acoust. Soc. Am. **103**, 962–972.

Macdonald, H. M. (**1902**). *Electric Waves* (University Press, New York).

Maekawa, Z. (**1968**). "Noise reduction by screens," Appl. Acoust. **1**(3), 157–173.

Mankbadi, R. R., and Uribe, J. F. (**2025**). "Perturbation solution for jet noise reduction via an air-water curtain," Phys. Fluids **37**, 113336.

Martens, S., and Spyropoulos, J. T. (**2010**). "Practical jet noise reduction for tactical aircraft," in *Proceedings of ASME Turbo Expo 2010: Power for Land, Sea and Air*, Glasgow, UK, June 14–18.

Mathews, L. T., and Gee, K. L. (**2024**). "Acoustical holography and coherence-based noise source characterization of an installed F404 engine," AIAA J. **62**(6), 2186–2199.

McIver, P., and Rawlins, A. D. (**1995**). "Diffraction by a rigid barrier with a soft or perfectly absorbent end face," Wave Motion **22**, 387–402.

McKinley, R. L., Bjorn, V. S., and Hall, J. A. (**2005**). "Improved hearing protection for aviation personnel," *New Direction for Improving Audio Effectiveness*, RTO-MP-HFM-123, Paper 13 (RTO, Neuilly-sur-Seine, France).

Menounou, P., and Asimakopoulos, V. (**2021**). "Empirical formulas for predicting the insertion loss behind wedges," Appl. Acoust. **182**, 108166.

Menounou, P., Busch-Vishniac, I. L., and Blackstock, D. T. (**2000**). "Directive line source model: A new model for sound diffraction by half planes and wedges," J. Acoust. Soc. Am. **107**, 2973–2986.

Menounou, P., Salagas, S., and Nikolaou, P. (**2025**). "Empirical formulas for the prediction of the diffraction field around rigid, absorbing, single or multiple wedges," Appl. Acoust. **233**, 110592.

Minnaert, M. (**1933**). "On musical air-bubbles and the sounds of running water," London, Edinburgh, Dublin Philosoph. Mag. J. Sci. **16**(104), 235–248.

Nikolaou, P., and Menounou, P. (**2024**). "Sound diffraction by knife-edges of finite length: Integral solution, dimensionless parameters, and explicit formulas," J. Acoust. Soc. Am. **155**, 1719–1734.

Office of Naval Research (**2025**). "Non-wearable and off-engine jet noise reduction," STTR 25.A-N25A-T021 (ONR, Washington, DC).

Olaveson, O., Ward, J. A., Johnson, J. P., Gee, K. L., and Wall, A. T. (**2022**). "Analysis of spatiospectral lobes in installed F404 engine noise radiation," in *Proceedings of the 28th AIAA/CEAS Aeroacoustics Conference*, Southampton, UK.

Olaveson, T. W., and Gee, K. L. (**2024**). "Wavelet-based characterization of spatiospectrotemporal structures in F404 engine jet noise," AIAA J. **62**(11), 4399–4410.

22 November 2026 18:10:11

Olaveson, T. W., and Gee, K. L. (**2025**). "Multiple wavepacket decomposition of F404 engine military jet noise," in *Proceedings of the AIAA Aviation Forum*, Las Vegas, NV.

Olaveson, T. W., and Gee, K. L. (**2026**). "Sound power from a collection of monopoles with arbitrary coherence: Theory and application to aeroacoustic noise sources," J. Acoust. Soc. Am. **159**, 1036–1047.

Olaveson, T. W., Gee, K. L., and Meadows, J. W. (**2025**). "Exploring the use of a curtain of bubbly water as a jet noise reduction mechanism," in *Proceedings of the 189th Meeting of the Acoustical Society of America*, Honolulu, HI.

Padois, T., Gauthier, P.-A., and Berry, A. (**2014**). "Inverse problem with beamforming regularization matrix applied to sound source localization in closed wind-tunnel using microphone array," J. Sound Vib. **333**, 6858–6868.

Papamoschou, D. (**2011**). "Wavepacket Modeling of the Jet Noise Source," in *Proceedings of the 17th AIAA CEAS Aeroacoustics Conference*, AIAA Paper No. 2011-2835.

Patel, T. K., and Viswanath, K. (**2026**). "Fundamental study of the transmission loss of jet noise through water curtains," *AIAA SciTech Forum*, Orlando, FL.

Pierce, A. D. (**1974**). "Diffraction of sound around corners and over wide barriers," J. Acoust. Soc. Am **55**, 941–955.

Prosperetti, A. (**1977**). "Thermal effects and damping mechanisms in the forced radial oscillations of gas bubbles in liquids," J. Acoust. Soc. Am. **61**, 17–27.

Smith, J. P., Burdisso, R. A., Fuller, C. R., and Gibson, R. G. (**1996**). "Active control of low-frequency broadband jet engine exhaust noise," Noise Control Eng. J. **44**(1), 45–52.

Sommerfeld, A. (**1896**). "Mathematische theorie der diffraction" ("Mathematical theory of diffraction"), Math. Ann. **47**, 317–374.

Van Wijngaarden, L. (**1968**). "On the equations of motion for mixtures of liquid and gas bubbles," J. Fluid Mech. **33**, 465–474.

Van Wijngaarden, L. (**1972**). "One-dimensional flow of liquids containing small gas bubbles," Annu. Rev. Fluid Mech. **4**, 369–394.

Wall, A. T., Gee, K. L., Morris, P. J., Colonius, T., and Lowe, K. T. (**2022**). "Introduction to the special issue on supersonic jet noise," J. Acoust. Soc. Am. **151**, 806–816.

Wever, E. G., and Bray, C. W. (**1936**). "The nature of bone conduction as shown in the electrical response of the cochlea," in *Proceedings of the Sixty-Ninth Annual Meeting of the American Otological Society*.

Wong, R., Richarz, W., and Ribner, H. (**2012**). "Shielding concepts for jet noise," in *Proceedings of the 7th Aeroacoustics Conference*, October 5–7, Palo Alto, CA.

Yanpeng, W., Yinghou, J., and Zhaobo, C. (**2018**). "Research on the well at the top edge of noise barrier," Appl. Acoust. **133**, 118–122.

22 November 2026 18:10:11